SINTEF
PROCEEDINGS 6

14th International Conference on CFD in
Oil & Gas, Metallurgical and Process Industries
SINTEF, Trondheim, Norway, October 12–14, 2020

Proceedings from the 14th International Conference on CFD in Oil & Gas, Metallurgical and Process Industries

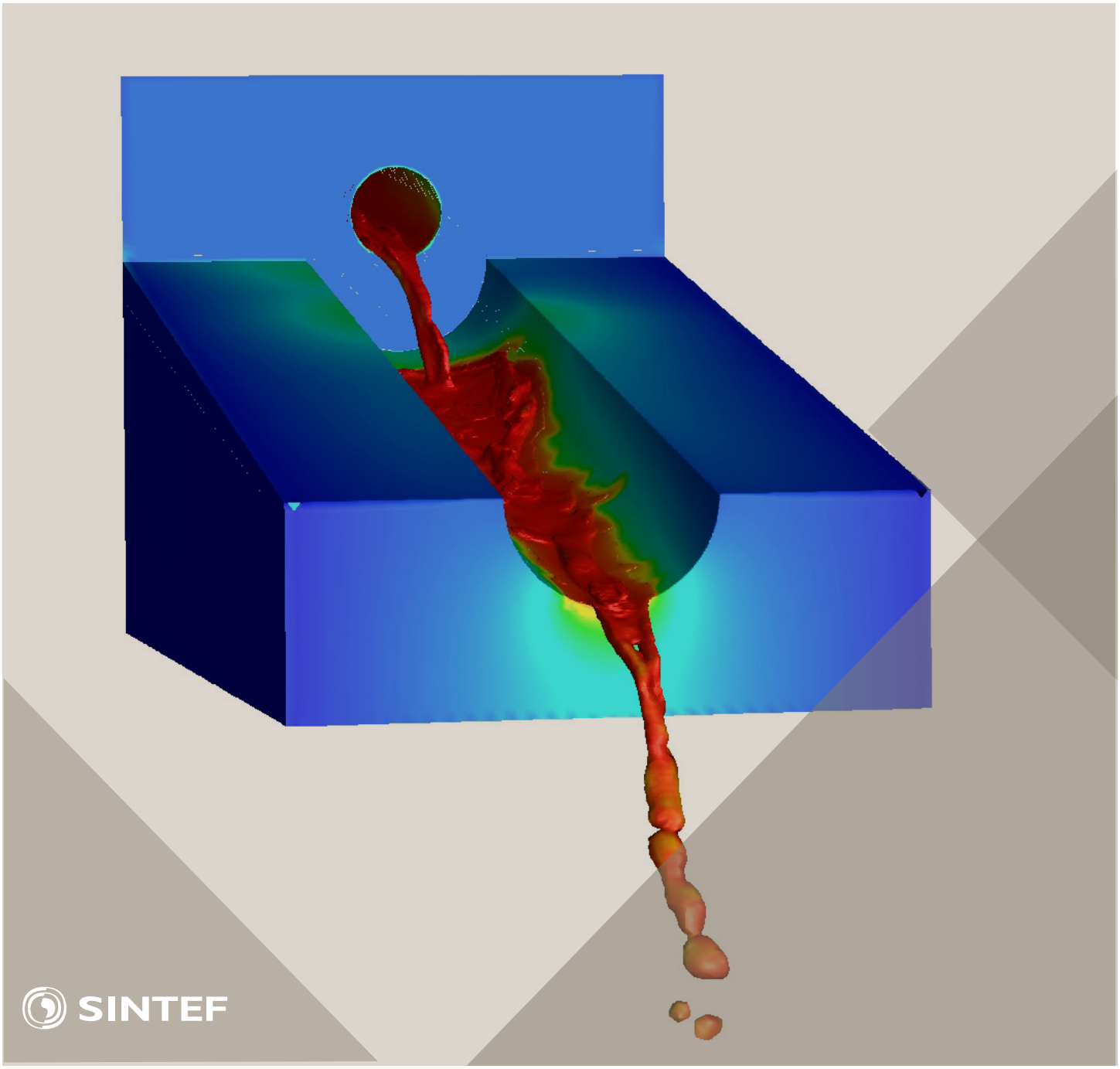

SINTEF Proceedings

Editors:
Jan Erik Olsen, Jan Hendrik Cloete and Stein Tore Johansen

Proceedings from the 14th International Conference on CFD in Oil & Gas, Metallurgical and Process Industries

SINTEF, Trondheim, Norway
October 12–14, 2020

SINTEF Academic Press

SINTEF Proceedings 6
Editors: Jan Erik Olsen, Jan Hendrik Cloete and Stein Tore Johansen

Proceedings from the 14th International Conference on CFD in Oil & Gas, Metallurgical and Process Industries, SINTEF, Trondheim, Norway, October 12–14, 2020

Keywords:
CFD, fluid dynamics, modelling

Cover illustration: Tapping of metal by Jan Erik Olsen

ISSN 2387-4295 (online)
ISBN 978-82-536-1684-1 (pdf)

SINTEF Academic Press
Address: Børrestuveien 3
PO Box 124 Blindern
N-0314 OSLO
Tel: +47 40 00 51 00

www.sintef.no/community
www.sintefbok.no

14th International Conference on CFD in Oil & Gas, Metallurgical and Process Industries
SINTEF, Trondheim, NORWAY
October 12-14, 2020

TOWARD COMPUTATIONAL MODELS OF ARC DYNAMICS IN SILICON SMELTERS

Quinn Gareth REYNOLDS
Mintek, Private Bag X3015, Randburg 2125, South Africa
University of Stellenbosch, Private Bag X1, Matieland, Stellenbosch 7602, South Africa
E-mail: quinnr@mintek.co.za

ABSTRACT
The production of silicon in electric smelting furnaces is a complex and energy-intensive process. High current plasma arcs are used in such furnaces to generate the temperatures required for the chemical reaction of silica to silicon. In order to facilitate further study of such processes, a computational magnetohydrodynamic model suitable for studying the electrical and dynamic behaviour of alternating current plasma arcs at industrial scales is described. An implementation of the model in the OpenFOAM® computational mechanics framework is developed, tested, and validated. A simulation workflow for prediction of practical aspects of furnace operation is demonstrated with a simple example calculation of the dependence of electrical parameters on electrode position for systems with multiple arcs in the presence of a test gas (Argon). It was found that the nonlinear electrical behaviour of the arc was exaggerated by the presence of multiple arcs, and that control of the furnace's voltage and current parameters by moving the electrodes could be negatively affected as a result.

Keywords: multiphysics, magnetohydrodynamics, plasma, pyrometallurgy .

NOMENCLATURE

Greek Symbols

α_R	Radiative absorption coefficient, $[1/m]$
δ_l	Mesh element size, $[m]$
ϵ_R	Radiative emission coefficient, $[1/m]$
ϕ	Electric potential, $[V]$
κ	Thermal conductivity, $[W/m.K]$
μ	Viscosity, $[Pa.s]$
μ_0	Vacuum permeability, $[N/A^2]$
ρ	Density, $[kg/m^3]$
σ	Electrical conductivity, $[1/\Omega m]$
$\bar{\bar{\tau}}$	Viscous stress tensor, $[N/m^2]$

Latin Symbols

$\mathbf{A}$	Magnetic vector potential, $[T.m]$
$\mathbf{B}$	Magnetic flux density, $[T]$
C_P	Heat capacity, $[J/kg.K]$
e	Elementary charge, $[C]$
$\mathbf{g}$	Gravitational acceleration, $[m^2/s]$
G	Radiative energy intensity, $[W/m^3]$
h	Specific enthalpy, $[J/kg]$
I	Current, $[A]$
$\mathbf{j}$	Current density, $[A/m^2]$
k_b	Boltzmann constant, $[J/K]$
L_a	Arc length, $[m]$
P	Pressure, $[Pa]$
q	Energy flux, $[W/m^2]$
Q	Energy source term, $[W/m^3]$
T	Temperature, $[K]$
$\mathbf{u}$	Velocity, $[m/s]$
V_a	Arc voltage, $[V]$

INTRODUCTION

During industrial production of silicon metal, the first stage in the process is the smelting of quartz ores containing silica (SiO_2) together with a mixture of carbonaceous reductants such as wood chips and metallurgical coke. This is generally performed in alternating current (AC) electric furnaces of circular design, using three vertically-mounted self-baking graphite electrodes. The raw materials are fed through the furnace roof and form a deep porous bed layer inside the containment vessel (the burden). An open cavity or "crater" is formed around the tip of each electrode inside the burden. Inside the crater, an electric arc operates between the tip of the electrode and the surface of the molten process products. High temperatures in the plasma arc (>10000°C) provide the required energy to drive the chemical reactions of SiO_2 to Si metal (Gasik, 2013). An illustration of a typical silicon furnace is shown in Figure 1.

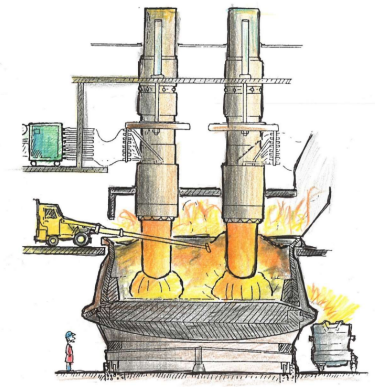

Figure 1: Layout and interior of a typical silicon smelter (image credit: Thorsteinn Hannesson, www.elkem.is).

A diagram of the crater region is shown in Figure 2. A unique feature of silicon processes is that the crater cavity is often surrounded by a shell of solid silicon carbide (SiC) which

forms as an intermediate reaction product. The conductive SiC layer provides an alternative current path between the electrode and the molten bath via one or more side arcs, which can operate in the upper part of the crater.

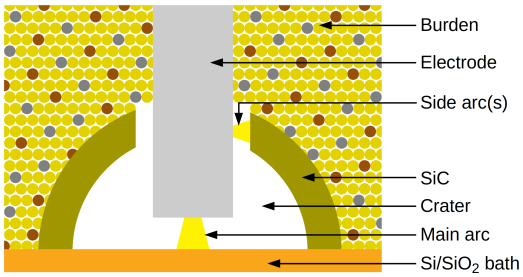

Figure 2: Structure of arc crater and surrounding burden.

Extensive work has been conducted in the development of numerical models for the study of arcs in pyrometallurgical furnaces. These generally fall into two distinct categories: *process models* which use simplified semi-empirical descriptions of the arc to capture observable phenomena such as overall energy balances and voltage-current relationships, and *computational models* which attempt to solve some or all of the fundamental governing equations of the plasma arc system in time and space. Examples of the former include channel arc models (Larsen, 1996) (Sævarsdóttir *et al.*, 1998) (Sanchez *et al.*, 2009), and arc shape models (Bowman and Krüger, 2009). Computational models have been continuously developed since the 1980s and modern multiphysics models may include power supply and transformer interaction effects (Sævarsdóttir *et al.*, 2001) (Reynolds, 2018), sophisticated boundary conditions to account for plasma non-ideality in anode and cathode regions (Lowke *et al.*, 1997) (Sævarsdóttir *et al.*, 2006), and applications to high current industrial systems (Sævarsdóttir *et al.*, 2006). Recent work has also examined the current distribution between main and side arcs in the crater using multi-region models (Tesfahunegn *et al.*, 2018).

Because they are computationally cheap and can often be run in real time or better, process models are most useful in furnace design, operation, and control while computational models are usually reserved for academic research. However with sustained exponential growth in available computer power, it is becoming increasingly feasible to use full-featured computational models in the furnace design and operation space; the present work aims to develop and demonstrate a modelling framework which can form the basis for numerical experiment and virtual prototyping studies in the future.

MODEL DESCRIPTION

Plasma arcs are a coupled physical system arising from interactions between multiple distinct phenomena: fluid flow, heat transfer, electromagnetism, and chemical reactions. Governing equations for each of these phenomena must be described. In the case of fluid flow, this is the compressible Navier-Stokes and continuity equations, including the Lorentz source term for acceleration of the plasma by electromagnetic fields:

$$\frac{\partial(\rho\mathbf{u})}{\partial t} + \nabla\cdot(\rho\mathbf{u}\otimes\mathbf{u}) + \nabla P = \nabla\cdot\bar{\bar{\tau}} + \mathbf{j}\times\mathbf{B} - \rho\mathbf{g} \quad (1)$$

$$\frac{\partial\rho}{\partial t} + \nabla\cdot(\rho\mathbf{u}) = 0 \quad (2)$$

Heat transfer is described by the energy conservation equation and includes terms describing enthalpy transport by electrons, joule heating, thermal radiation, and mechanical heating. The complete energy equation is given by:

$$\frac{\partial(\rho h)}{\partial t} + \nabla\cdot(\rho\mathbf{u}h) = \nabla\cdot\left(\frac{\kappa}{C_P}\nabla h\right) + \nabla\cdot\left(\frac{5k_B h\mathbf{j}}{2eC_P}\right) + \frac{\mathbf{j}\cdot\mathbf{j}}{\sigma} - Q_r + Q_m \quad (3)$$

The enthalpy and pressure determine a unique temperature field, and (3) is therefore effectively an equation in T. The mechanical source Q_m includes standard terms for heating by pressure and kinetic energy changes in compressible flows (viscous dissipation is neglected). The thermal radiation source Q_r is a complex function of temperature, wavelength, and geometry, and must be obtained from an appropriate solution of the radiative transport equation. This is discussed further in the implementation sub-section.

The electromagnetic fields are governed by Maxwell's equations, presented here in the magnetic vector potential formulation using the Coulomb gauge. Significant simplifications are made by discarding second order time derivatives related to high-speed wave propagation dynamics:

$$\nabla\cdot\mathbf{j} = 0 \quad (4)$$

$$\nabla^2\mathbf{A} = -\mu_0\mathbf{j} \quad (5)$$

$$\mathbf{j} = -\sigma\left(\nabla\phi + \frac{\partial\mathbf{A}}{\partial t} - \mathbf{u}\times\mathbf{B}\right) \quad (6)$$

$$\mathbf{B} = \nabla\times\mathbf{A} \quad (7)$$

Here, the expression for the current density vector (6) and the relationship between the magnetic vector potential and the magnetic field (7) must be substituted into (4) and (5) to obtain governing equations for ϕ and $\mathbf{A}$ respectively.

In order to provide a closure for this set of equations, the local thermodynamic equilibrium approximation (Boulos *et al.*, 1994) is used - this is generally valid in plasma arcs away from the anode and cathode surfaces. This approximation assumes that chemical as well as thermal equilibrium exists between the electrons and heavy species (ions, atoms, molecules) and eliminates the need to perform computationally-costly chemical reaction dynamics calculations. With this approximation, plasma chemical compositions and thermophysical properties may be calculated in advance as functions of the thermodynamic state variables only.

Implementation details

For most cases of relevance to industrial furnace operations, equations (1)-(5) must be solved numerically. A variety of modern computational fluid dynamics (CFD) methods are available for this including finite difference, finite volume, and meshless methods such as smoothed particle hydrodynamics and lattice Boltzmann techniques. In the present work a finite volume method implementation was developed using the OpenFOAM® open source computational mechanics framework (OpenFOAM, 2019). Source code from version 7, sub-version 20191118 was used as a basis for the present work.

The implementation is based on the `rhoPimpleFoam` compressible flow solver included with standard releases of OpenFOAM®. This solver implements a segregated solution of the $\mathbf{u}$, P, and T fields, with a combined pressure-implicit with splitting of operators (PISO) and semi-implicit method for pressure-linked equations (SIMPLE) algorithm used for the CFD component.

As part of OpenFOAM®'s standard framework a number of interoperable numerical schemes are available for the finite-volume discretisation, together with shock-capturing limiters for transonic or supersonic flow cases. Although turbulence modelling was not applied in the present study a comprehensive framework is also present for this, and investigations into large-eddy simulation (LES) integration in arc models are currently underway.

The base solver was extended with a sub-module implementing solution of equations (4) and (5) for fields $\mathbf{A}$ and ϕ. The sub-module performs a loop solving the components of the magnetic vector potential and electric potential as segregated matrix equations, and iterating until the largest residual is below a specified value. This calculation is executed at each time step in a simulation, and the results are passed back to the CFD model via appropriate source terms in the momentum and energy equations. A simplified pseudo-code description of the electromagnetic solver algorithm is as follows:

```
...
calculate σ(P,T)
n_EM = 0
while n_EM < n_EM,max do
    solve equation (4) for φ
    store φ residual
    calculate j using equation (6)
    solve equation (5) for A components
    store A component residuals
    calculate B using equation (7)
    if φ and A residuals < specified tolerance then
        exit while loop
    end if
    n_EM++
end while
if n_EM,max reached then
    print convergence warning
end if
...
```

A new thermodynamics sub-module was developed in order to permit the specification of ρ, μ, C_P, κ, and σ as functions of temperature and pressure using lookup tables. For the results shown in the present paper, the properties (with the exception of the plasma density) were approximated as being invariant with pressure. A simple pseudo-compressible formulation was used which scales the density relative to a reference state in accordance with the ideal gas law:

$$\rho(T,P) = \frac{P}{P_0}\rho_0(T) \tag{8}$$

A comparison between the exact and ideal-gas scaled density was calculated for an argon plasma using the open source `minplascalc` Python package (minplascalc, 2018), and is shown in Figure 3. The agreement is very good in the weakly-compressible pressure range, with minor deviations occurring only at high temperatures when multiply-ionised species start to become significant. Although argon gas was used for all the simulations in the present work, it is expected that similar behaviour will be observed in more complex process gas plasmas.

A new absorption/emission sub-module for radiation modelling was also developed in order to allow α_R and ϵ_R to be specified as functions of temperature, pressure, and wavelength via lookup tables. For the work in this paper, the wavelength dependence was integrated out and the pressure

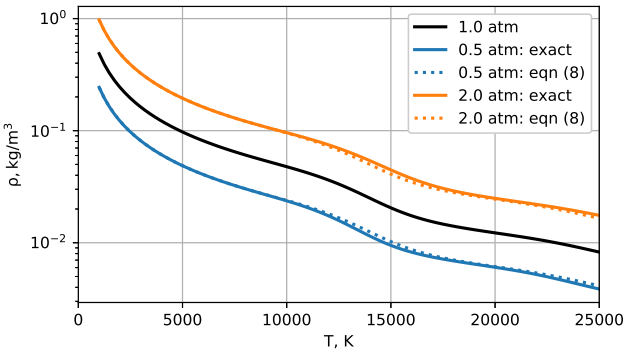

Figure 3: Comparison of ideal and pseudo-compressible density calculations for argon plasma near atmospheric pressure.

dependence neglected in order to obtain total coefficients as functions of temperature only. These are passed as arguments to any of OpenFOAM®'s standard radiation solver sub-models, which at present includes the P_1 (used here), discrete ordinate method, and view factor models. Provided reliable values of the emission and absorption coefficients are available, these sub-models alleviate the need to pre-calculate effective values of Q_R based on fixed geometries such as cylinders or spheres at the expense of some additional computational cost. At user-defined intervals (typically each time step) the chosen radiation model is solved using a segregated matrix solution algorithm, and the results are returned to the CFD model via a radiation intensity field.

Boundary conditions for ϕ

At cathode surfaces it is often expedient to specify a fixed current density in the region where the arc attaches (Bowman and Krüger, 2009). This is complicated in cases of time-varying currents and three dimensions, since the shape, size, and location of the arc attachment zone can vary arbitrarily. In the present model this was implemented by looping over a list of all surface elements on the cathode ordered by surface temperature, and assigning each to the attachment spot until the total required area for the current at that time is reached. The boundary condition per element is then assigned as follows:

$$\frac{\partial\phi}{\partial\mathbf{n}} = \begin{cases} -\frac{j_k}{\sigma} & \text{if } \in \text{ attachment zone} \\ 0 & \text{if } \notin \text{ attachment zone} \end{cases} \tag{9}$$

It should be noted that more rigorous cathode and anode boundary conditions are possible, such as those developed by Lowke *et al.* (1997) and Sævarsdóttir *et al.* (2006) which directly model the behaviour of the plasma in the near-electrode sheath. It is recommended to consider such approaches in future work, particularly at high currents.

Boundary conditions for $\mathbf{A}$

The solution of the magnetic vector potential equation (5) requires spatial boundary conditions to be specified. In complex geometries these are difficult to determine precisely, although Westermoen (2007) reports that acceptable accuracy may be obtained by setting the derivative in the direction normal to the boundary surface to zero while forcing the tangential components to zero (note that Westermoen's conclusions were based on qualitative comparisons from a sensitivity study using identical models with $\mathbf{A} = 0$ Dirichlet conditions at the boundary). This is equivalent to a "magnetically insulating"

boundary:

$$\frac{\partial\left(\mathbf{A}\cdot\mathbf{n}\right)}{\partial\mathbf{n}}=0,\mathbf{A}\cdot\mathbf{t}=0 \tag{10}$$

In the present implementation of the model this is achieved by pre-computing normal and tangent vector basis sets on each surface element in the geometry at the start of the simulation, and using a linear transformation to extract the required mixed boundary condition for each component of $\mathbf{A}$ in order to satisfy (10) on arbitrarily-oriented surfaces.

Boundary conditions for T

The anode and cathode surfaces in direct contact with the arc can receive extremely high energy fluxes from the hot plasma by conduction, convection, and radiation. This can raise the surface temperature to the point at which materials begin to evaporate. In the present model this is accounted for by numerically limiting the temperature that a surface can reach, with any excess energy assumed to be taken up by the phase change:

$$\begin{cases}-\kappa\frac{\partial T}{\partial\mathbf{n}}=q_b & \text{if } T<T_v\\ T=T_v & \text{if } T\geq T_v\end{cases} \tag{11}$$

Here, q_b is a combined expression which must account for any additional energy balances in the plasma sheath, surface radiation fluxes, energy of phase change, and energy transport into the surface by conduction or other mechanisms. In the present work this is simplified by assuming the electrode surface is in thermal equilibrium ($q_b \approx 0$) with the neighbouring plasma unless it is over the vaporisation temperature T_v. More rigorous approaches are documented in for example Pálsson *et al.* (2007) and Sævarsdóttir *et al.* (2006), and should be considered in future models.

RESULTS AND DISCUSSION

In silicon smelters, the main and side arcs typically operate at short lengths (< 15 cm) on the surface of very large electrodes (> 1.5 m). To a first approximation the arc is effectively contained between two parallel surfaces serving as cathode and anode. For the present study a simplified three-dimensional geometry was therefore used to represent the region in the immediate vicinity of the arc, and is shown in Figure 4.

The disc-shaped region is bounded by four surfaces: the *anode*, representing the molten bath or SiC surface, the *cathode*, representing the portion of the graphite electrode that the arc is allowed to attach in, the *electrode*, representing the remainder of the electrode surface, and the *open boundary* which permits inflow and outflow from the surrounding gas atmosphere in the crater. The anode, cathode, and electrode boundaries are treated as no-slip walls. The anode is held at ground potential (0 V), while the cathode boundary is specified dynamically during the simulation according to equation (9) taking into account the changing values of σ and $\mathbf{j}$ in time. An average cathode current density of j_k = 10^7 A/m^2 representative of diffuse arc attachments was assumed based on results of simulations by Sævarsdóttir *et al.* (2006). All other boundaries are treated as insulating, with a zero-gradient condition applied to ϕ. The cathode and electrode are limited in temperature to the sublimation temperature of graphite, 4100 K. The anode is similarly regulated to 3000 K representing the vaporisation temperature of either molten silica slag or solid SiC.

In the present work, the arc is assumed to be supplied with a perfectly sinusoidal current at 50 Hz. This is a simplification - in general, there will always be some degree of interaction

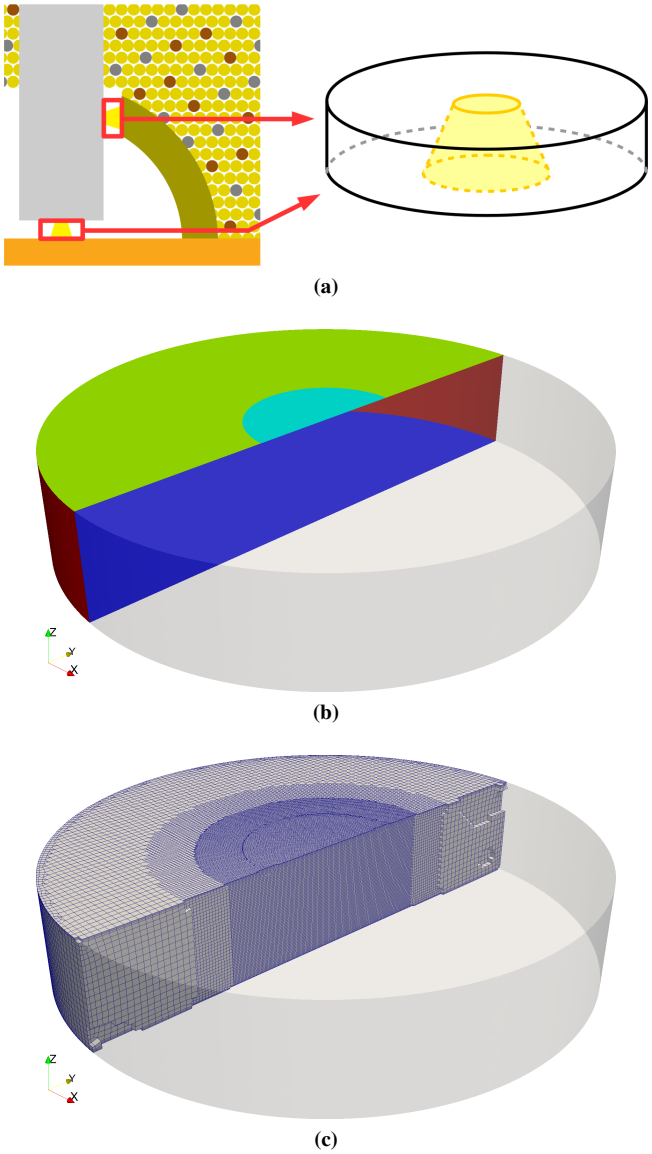

Figure 4: (a) Crater region showing model domains for arcs, (b) model region showing cathode (light blue), electrode (green), anode (dark blue) and open boundaries (red), and (b) example computational mesh showing local refinements.

between the arcs and the three-phase transformer feeding the furnace (Sævarsdóttir *et al.*, 1998). However due to the significant line inductances present the current waveforms generally remain much more sinusoidal than the voltage. There is also a superimposed magnetic field generated by the three electrodes which causes the arcs to be deflected away from the furnace centreline, but the examination of this effect is left for a future study.

For all simulations shown in the subsequent sections, argon gas was used as the plasma medium. Argon plasmas are well-studied both experimentally and theoretically, and serve as a good basis for understanding the model's trends and general behaviour before extending to specific Si-C-O atmospheres typical of silicon furnaces. Plasma property data was obtained from Boulos *et al.* (1994) or calculated using minplascalc (2018).

A second-order linear Gauss finite volume discretisation was used for the spatial component of all field variables, with the exception of velocity (limited linear TVD scheme) and enthalpy (upwind scheme). A backward Euler scheme was

used for the temporal discretisation, combined with adaptive time-step calculation to limit the Courant number to below 1. The numerical parameters for the field matrix solvers are shown in Table 1, and were used in all simulations unless otherwise indicated.

Table 1: Numerical settings for OpenFOAM® plasma arc simulations

Field variable	Matrix solver	Preconditioner	Residual tolerance
P	PCG	GAMG	10^{-6}
$\mathbf{u}$	smoothSolver	n/a	10^{-7}
G	PCG	GAMG	10^{-5}
ϕ	PCG	GAMG	10^{-6}
$\mathbf{A}$	PCG	GAMG	10^{-5}

Model validation

The computational model was validated against experimental data from Larsen (1996). The current supplied in the experiment was 650 A RMS, and the arc length was 4 cm. A computational model with a volume-element resolution δ_l of 1 mm was used. The model was run for a total of 0.1 s starting from stagnant conditions (zero velocity, uniform temperature of 10000 K), with the experimental data compared against a cycle from the second half of the simulation after the initial conditions had decayed sufficiently. The results are shown in Figure 5.

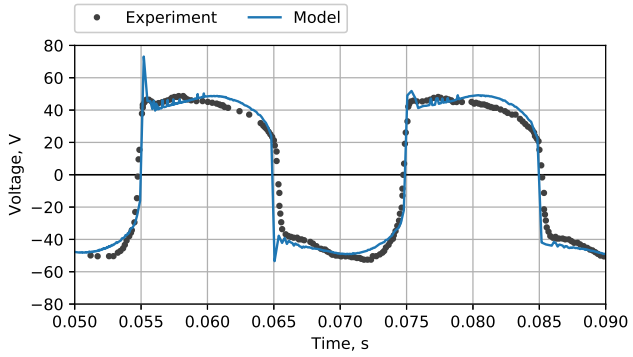

Figure 5: Comparison between experimental and model voltages for a laboratory AC arc in argon gas.

Relatively good agreement was obtained between model and experiment. In particular the RMS voltages (42.7 V for the experiment, 44.2 V for the model) match closely, and the qualitative shape of the voltage waveform is quite well captured. The differences seen are mostly high-frequency disturbances of short duration - it is possible that these are due to numerical noise in the model, or they may be real physical phenomena which are damped out by the experimental system's circuit inductance.

Mesh dependence

In order to investigate the model's accuracy on computational meshes of different resolutions, a series of argon arc simulations was performed using both the validation test case, 4 cm arc length and 650 A current, and a case close to industrial scale, 10 cm arc length and 42 kA current (for comparison, typical silicon smelters operate with arcs < 15 cm in length and between 50 and 100 kA current). The mesh resolution in the central arc region was varied in both cases, and the final two cycles of the 0.1 s simulation period were compared.
Results for the validation case are shown in Figure 6. It can be seen that the voltages predicted by the computational model are fairly insensitive to mesh resolution in this range, with values and qualitative dynamic behaviour being captured reasonably well at all resolutions.

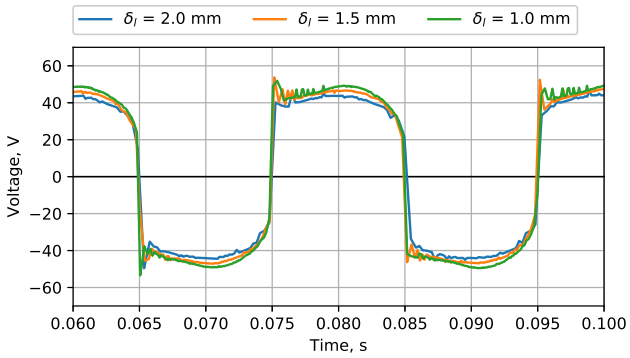

Figure 6: Model voltages at different mesh resolutions for a 4 cm arc at 650 A RMS.

For the industrial-scale case there is a transition in the resolved dynamics as the spatial resolution increases. As seen in Figure 7, although the model voltages are again not particularly sensitive to mesh resolution, there is significantly more high-frequency behaviour in the voltage during the peak current periods on finer meshes. Whether the source of this noise is numerical or physical requires further investigation, however, high-frequency dynamics have been observed in industrial arcs under different conditions (Hockaday *et al.*, 2015).

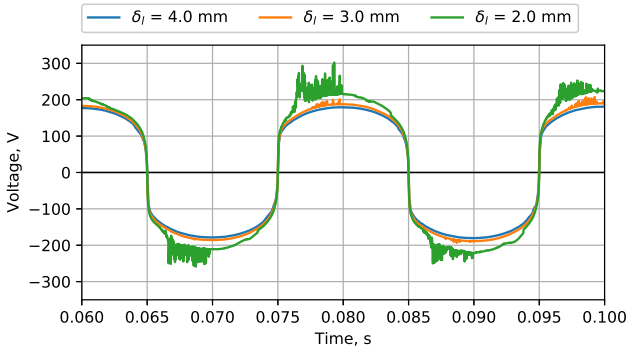

Figure 7: Model voltages at different mesh resolutions for a 10 cm arc at 42 kA RMS.

Industrial-scale arc characterisation

As a simple demonstration of the utility of computational models in studying practical furnace matters, the problem of *arc characteristics* is considered. In industrial silicon smelters the electrodes are typically mounted on mechanical or hydraulic hoists, and their position on the vertical axis is constantly adjusted by automated control systems. The power input to the furnace as well as the electrical balance between the three electrodes is maintained in this fashion in order to ensure consistent operation of the unit.
The relationship between electrode position, current, and voltage can be quite complex for AC arcs. This is further exacerbated if side arcs are present between the electrode and the SiC shell around the crater, since multiple parallel current paths to the neutral point are then possible (Tesfahunegn *et al.*, 2018). Moving the electrode changes the arc length of the main arc but has minimal effect on the side arcs; it is therefore expected that as the electrode is raised the balance

of current distribution will shift from main to side arcs. This is shown schematically in Figure 8.

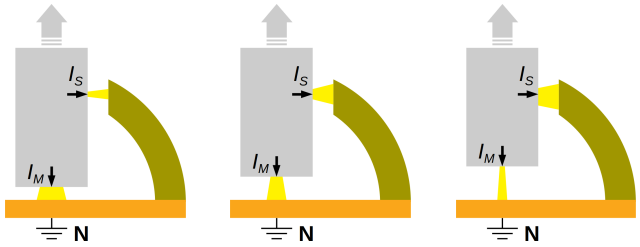

(a) $I_M > I_S$ (b) $I_M \approx I_S$ (c) $I_M < I_S$

Figure 8: Redistribution of current between main and side arcs as electrode is raised (l to r).

In order to demonstrate a methodology for quantifying such effects, the computational model was used to estimate the voltage response of an argon plasma arc over a range of electrode currents and arc lengths approximating the scale of industrial silicon furnaces - 0 to 71 kA RMS, and 0 to 10 cm. Visualisations of selected simulation results at different extremes of current and arc length are shown in Figure 9. These simulations were performed on meshes with 2 mm resolution in the central arc regions.

The voltage dynamics of the arc are shown in Figure 10 for some example cases. It can be seen that the voltage is strongly dependent on arc length and less sensitive to current, which is in line with predictions from empirical process models. As the arc length decreases, the voltage waveforms also become more rectangular and less sensitive to current. This is related to the shape of the conductive core of the arc, which tends toward cylindrical at higher currents and lower arc lengths.

AC voltages were calculated for each of the 25 cases simulated during the arc characterisation study, and are given in Table 2. In order to facilitate faster processing and use in real-time applications, the voltage results from the computational model were fitted to a simple empirical expression given in equation (12) (for currents in kA and arc length in cm). This expression has a maximum error of 6% relative to the values in Table 2, and is shown graphically in Figure 11.

Table 2: RMS voltages from arc characterisation simulations

	L_a 2 cm	L_a 4 cm	L_a 6 cm	L_a 8 cm	L_a 10 cm
I 14 kA	46.3	74.8	97.3	112.7	125.9
I 28 kA	49.8	84.4	108.3	131.1	151.2
I 42 kA	55.3	88.8	116.6	149.5	175.0
I 57 kA	55.9	92.4	123.4	167.3	194.0
I 71 kA	56.5	93.5	131.9	179.0	208.7

$$
\begin{aligned}
C_1 &= 72.9\left(1 - e^{-0.424 L_a}\right) + 4.29 L_a \\
C_2 &= \frac{1.45}{1 + e^{-0.755(L_a - 6.47)}} - 0.0109 \\
V_a\left(I, L_a\right) &= C_1\left(1 - e^{-0.194 I}\right) + C_2 I
\end{aligned}
\tag{12}
$$

When main and side arcs are both present in the system, the total electrode current must divide between them. Assuming that the graphite of the electrode and the SiC of the crater shell are both very conductive, this implies that the arc voltages must all be approximately equal. If I_{tot} (= $I_M + I_S$), $L_{a,M}$, and $L_{a,S}$ as well as the number of separate side and main arcs are known, the current balance can be solved simply by equating the main and side arc voltages $V_{a,M}$ and $V_{a,S}$, both of which are given by equation (12).

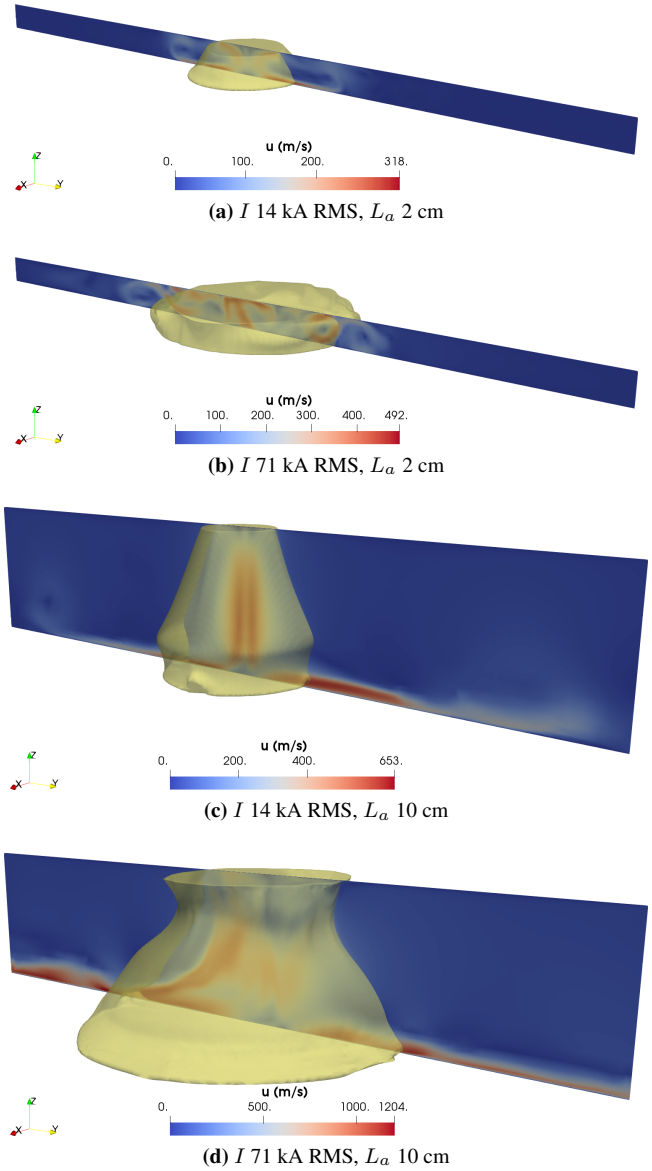

(a) I 14 kA RMS, L_a 2 cm

(b) I 71 kA RMS, L_a 2 cm

(c) I 14 kA RMS, L_a 10 cm

(d) I 71 kA RMS, L_a 10 cm

Figure 9: Velocity magnitude (plane) and temperature (8500 K isotherm) fields visualised at 0.1 s for selected arc characterisation simulations.

An example calculation using the present demonstration case is shown in Figure 12. In this example, only a single main and side arc were assumed to be present. The clearance between the electrode and the SiC shell is $L_{a,S}$ = 5 cm.

Several effects are apparent. Firstly, the arc system in a silicon furnace crater is likely to be a very nonlinear and non-ohmic circuit element. This has implications for the electrical design, scale-up, and operation of furnace plants.

Second, it is clear that there will be a loss of control sensitivity in the region where the main arc is longer than the side arcs. Beyond this point, changing the electrode position has less and less effect on the electrode voltage since the majority of the electrode current is being carried by the side arcs. Such an arrangement has the potential to cause runaway raising of electrodes if naive control implementations are used.

Finally, a simple means of extinguishing any side arcs is available should it become necessary to do so. Lowering the electrode into the molten bath would drop the side arc current close to zero, leaving only the main arc running when the electrode is raised again. Whether the transformers on real furnace plants are able to tolerate dead-shorting a phase to

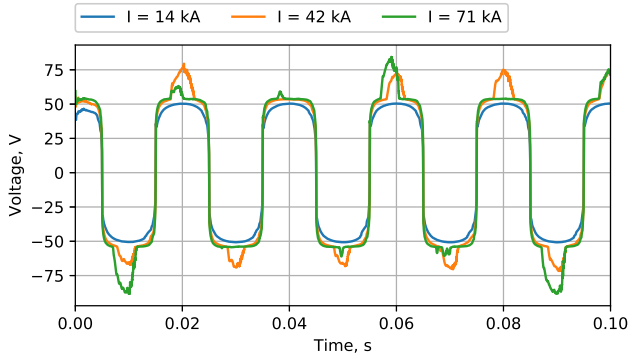

(a) L_a 2 cm

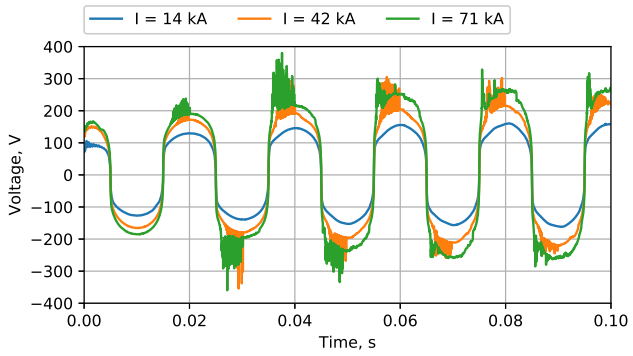

(b) L_a 10 cm

Figure 10: Evolution of arc voltage for selected arc characterisation simulations.

neutral on a routine basis would however need to be considered carefully.

CONCLUSION

A flexible and extensible computational model suitable for studying the dynamic behaviour of AC plasma arcs in silicon smelter environments was successfully developed. A preliminary validation study was conducted against data from small-scale experimental tests, with good agreement. An example workflow for the calculation of arc characteristics at industrial scale was demonstrated using arcs operating in argon gas plasmas, by combining a suite of arc simulations with empirical system modelling to account for the presence of main and side arcs and their influence on the complex nonlinear relationships between electrode position, voltage, and current.

This work represents a preliminary step, and of course much remains to be done in order to make the plasma arc model more applicable to industrial systems. The model will need to be tested more thoroughly both for numerical veracity and validity against additional experimental and industrial data, both of which are currently in progress. The assembly of a database of appropriate thermophyiscal properties for Si-C-O plasma mixtures for use in computational simulations is also underway and will be applied in a future study. Improvements in the boundary conditions used, particularly at the conducting surfaces, should be explored to ensure that non-ideality effects in near-surface plasma sheaths are captured correctly. Similarly, the interaction between the arcs and the transformers powering them should be included in the computational model using appropriate three-phase circuit calculations to avoid any errors arising from specifying the current waveform directly. Energy transport and electromagnetic fields in

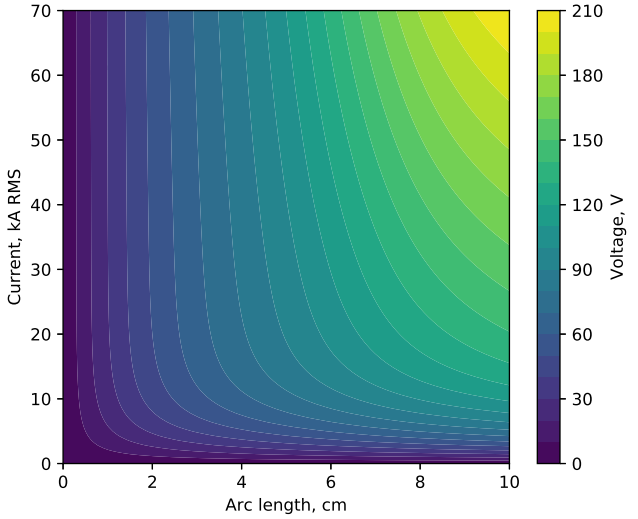

Figure 11: Relationship between current, arc length, and voltage described by equation (12).

the solid materials comprising the arc crater region should also be accounted for via improved boundary conditions or multi-region models. For large-scale arcs the use of turbulence modelling methods is advisable to optimise computational workloads, and these will require separate verification and validation to determine their applicability to multiphysics plasma arc problems. Finally, the coupling of the plasma arc models with additional relevant physics such as multiphase fluid flow in the molten bath should be considered, as it is expected that these will have an appreciable effect on the system's dynamic behaviour.

ACKNOWLEDGEMENTS

This paper is published by permission of Mintek. The author acknowledges the Centre for High Performance Computing (CHPC), South Africa, for providing computational resources to this research project. Discussions with colleagues at the University of Reykjavík on the subject of computational arc modelling were greatly appreciated.

REFERENCES

BOULOS, M.I., FAUCHAIS, P. and PFENDER, E. (1994). *Thermal Plasmas: Fundamentals and Applications*, vol. 1. Plenum Press, New York, USA.

BOWMAN, B. and KRÜGER, K. (2009). *Arc Furnace Physics*. Verlag Stahleisen GmbH, Düsseldorf, Germany.

GASIK, M. (ed.) (2013). *Handbook of Ferroalloys*. Elsevier Ltd, United Kingdom.

HOCKADAY, C.J., REYNOLDS, Q.G. and JORDAN, D.T. (2015). "Industrial demonstration of arc detection in DC arc furnaces". *Proceedings of the Fourteenth International Ferroalloys Congress: Energy Efficiency and Environmental Friendliness are the Future of the Global Ferroalloy Industry*, 682–688. Public Organization INFACON XIV, Kyiv, Ukraine.

LARSEN, H.L. (1996). *AC electric arc models for a laboratory set-up and a silicon metal furnace*. Dr. Ing., Norwegian University of Science and Technology (NTNU), Trondheim, Norway.

LOWKE, J.J., MORROW, R. and HAIDAR, J. (1997). "A simplified unified theory of arcs and their electrodes". *Journal of Physics D: Applied Physics*, **30(14)**, 2033–2042.

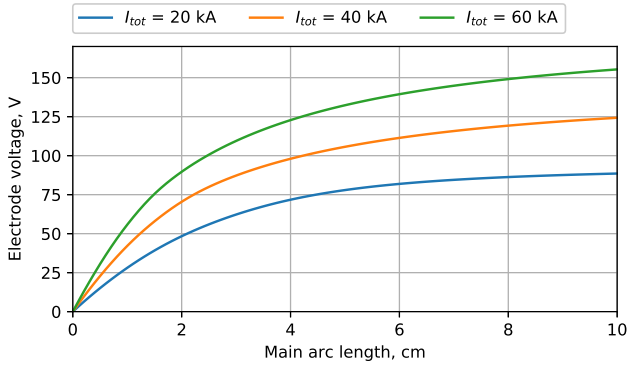

(a) Voltages

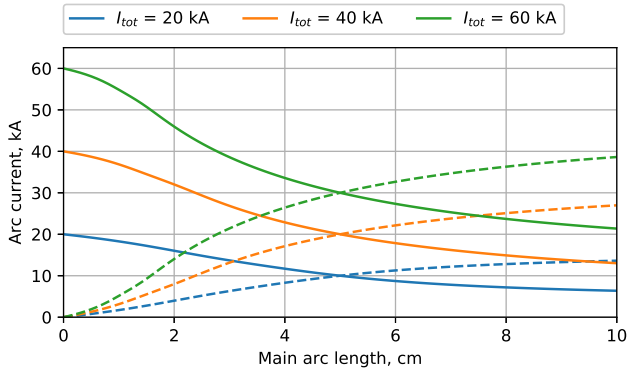

(b) Main (solid lines) and side (dashed) arc currents

Figure 12: Electrical behaviour of example system as a function of main arc length $L_{a,M}$ ($\propto$ electrode position) for different values of I_{tot}.

MINPLASCALC (2018). "minplascalc v0.7 alpha, commit 22a5f5d". URL `https://github.com/quinnreynolds/minplascalc`.

OPENFOAM (2019). "OpenFOAM v7". URL `https://openfoam.org/release/7/`.

PÁLSSON, H., SÆVARSDÓTTIR, G.A., JÓNSSON, M.T. and BAKKEN, J.A. (2007). "Thermal effects on carbon based electrodes close to a high current electric arc". *INFACON XI 2007: Innovations in Ferroalloys Industry*, 695–702. IFAPA, New Delhi, India.

REYNOLDS, Q.G. (2018). "Influence of the power supply on the behaviour of DC plasma arcs - a modelling study". *Journal of the Southern African Institute of Mining and Metallurgy*, **118(6)**, 655–660.

SÆVARSDÓTTIR, G.A., LARSEN, H.L. and BAKKEN, J.A. (1998). "Modelling of AC Arcs in Three-Phase Submerged Arc Furnaces". *8th International Ferroalloys Congress Proceedings*, 317–322. China Science & Technology Press, Beijing, China.

SÆVARSDÓTTIR, G.A., BAKKEN, J.A., SEVASTYANENKO, V.G. and GU, L. (2001). "Arc Simulation Model for Three-Phase Electro-Metallurgical Furnaces". *The Ninth International Ferroalloys Congress and the Manganese 2001 Health Issues Symposium Official Proceedings*, 253–263. The Ferroalloys Association, Quebec City, Canada.

SÆVARSDÓTTIR, G.A., PÁLSSON, H., JÓNSSON, M.T. and BAKKEN, J.A. (2006). "Electrode Erosion due to High-Current Electric Arcs in Silicon and Ferrosilicon Furnaces". *Steel Research International*, **77(6)**, 385–391.

SANCHEZ, J.L.G., RAMÍREZ-ARGAEZ, M.A. and CONEJO, A.N. (2009). "Power Delivery from the Arc in AC Electric Arc Furnaces with Different Gas Atmospheres". *Process Metallurgy*, **(2)**, 113–120.

TESFAHUNEGN, Y.A., MAGNUSSON, T., TANGSTAD, M. and SÆVARSDÓTTIR, G.A. (2018). "Effect of electrode shape on the current distribution in submerged arc furnaces for silicon production - A modelling approach". *Journal of the Southern African Institute of Mining and Metallurgy*, **118(6)**, 595–600.

WESTERMOEN, A. (2007). *Modelling of Dynamic Arc Behaviour in a Plasma Reactor*. Ph. D., Norwegian University of Science and Technology (NTNU), Trondheim, Norway.